Room temperature aqueous-based synthesis of copper-doped lead sulfide nanoparticles for thermoelectric application

Mengyao Li,[a] Yu Liu,*[,b,c] Yu Zhang,[a] Cheng Chang,[b] Ting Zhang,[d] Dawei Yang,[a] Ke Xiao,[a] Jordi Arbiol,[d,e] Maria Ibáñez,[b] Andreu Cabot*[, a,e]

[a] *Catalonia Energy Research Institute - IREC, Sant Adrià de Besòs, 08930 Barcelona, Spain.*

[b] *Institute of Science and Technology Austria (IST Austria), Am Campus 1, 3400, Klosterneuburg, Austria.*

[c] *School of Chemistry and Chemical Engineering, Hefei University of Technology, Hefei 230009, China.*

[d] *Catalan Institute of Nanoscience and Nanotechnology (ICN2), CSIC and BIST, Campus UAB, Bellaterra, 08193 Barcelona, Catalonia, Spain.*

[e] *ICREA, Pg. Lluis Companys 23, 08010 Barcelona, Catalonia, Spain.*

**Corresponding author: E-mail: yliu@hfut.edu.cn; acabot@irec.cat.*

ABSTRACT

A versatile, scalable, room temperature and surfactant-free route for the synthesis of metal chalcogenide nanoparticles in aqueous solution is detailed here for the production of PbS and Cu-doped PbS nanoparticles. Subsequently, nanoparticles are annealed in a reducing atmosphere to remove surface oxide, and consolidated into dense polycrystalline materials by means of spark plasma sintering. By characterizing the transport properties of the sintered material, we observe the annealing step and the incorporation of Cu to play a key role in promoting the thermoelectric performance of PbS. The presence of Cu allows improving the electrical conductivity by increasing the charge carrier concentration and simultaneously maintaining a large charge carrier mobility, which overall translates into record power factors

at ambient temperature, 2.3 $mWm^{-1}K^{-2}$. Simultaneously, the lattice thermal conductivity decreases with the introduction of Cu, leading to a record high ZT = 0.37 at room temperature and ZT = 1.22 at 773 K. Besides, a record average ZT_{ave}=0.76 is demonstrated in the temperature range 320-773 K for n-type $Pb_{0.955}Cu_{0.045}S$.

Keywords: PbS, aqueous synthesis, nanoparticles, thermoelectricity, copper-doping.

1. Introduction

Thermoelectric devices allow the solid-state conversion between thermal and electrical energy. Their energy conversion efficiency is in large part determined by the charge and heat transport properties of the thermoelectric material [1–4]. The key transport properties of the material are grouped within a dimensionless figure of merit, $ZT=S^2\sigma T/\kappa$, with S, σ, T, and κ representing the Seebeck coefficient, electrical conductivity, absolute temperature, and thermal conductivity, respectively. Several strategies have been proposed to increase the thermoelectric figure of merit, including the maximization of the power factor ($PF=S^2\sigma$) through optimizing the charge carrier concentration and mobility [5–9] and adjusting the electronic band structure [10,11], and to reduce the thermal conductivity by introducing multi-scale phonon scattering centers, including lattice defects and grain boundaries [12–18]. In addition to the engineering of high-performance thermoelectric materials, to ensure the commercial viability of thermoelectric devices, research work should also be devoted to the development of low-cost synthetic procedures and the use of materials based on earth-abundant elements.

Among the plethora of proposed compounds, PbS is regarded as a paradigmatic thermoelectric

material for medium-temperature applications owing to its simple binary composition, moderate cost and notable performance. However, pure and crystalline PbS is characterized by a relatively high lattice thermal conductivity and modest power factors, which can be improved through nanostructural engineering and doping [19-29]. The nanostructural engineering of PbS is an effective strategy to lower its lattice thermal conductivity through intensifying phonon scattering, while at the same time optimizing the carrier effective mass (m^*). Besides, extrinsic dopants can contribute to tuning the charge carrier concentration (n) towards maximizing the material power factor.

In particular, Cu doping has been used to control the PbS charge carrier concentration and reduce its thermal conductivity [23,26,30,31]. The role of Cu strongly depends on its location within the PbS lattice, its concentration and the presence of additional impurities defining the PbS conductivity type. Generally, interstitial Cu is considered an n-type dopant and substitutional Cu is considered a p-type dopant. Cu has been also proposed to occupy Pb sites by filling Pb vacancies, thus reducing the hole concentration [26]. Besides, the presence of Cu^+ ions within the lattice can lead to the formation of S vacancies that would increase the concentration of free electrons, as frequently observed in Cu_xS compounds [32,33]. Even more complicated, Cu may occupy different locations at different temperature ranges, resulting in what has been named dynamic doping. Indeed, Cu atoms occupying interstitial sites at low temperatures have been reported to replace Pb at higher temperatures, thus evolving from an electron injector to an electron trap [23].

Nanostructured PbS is frequently produced by a three-step top-down approach involving a solid-state reaction, ball milling, and nanopowder consolidation. PbS nanomaterials are also

produced by a two-step bottom-up approach involving the synthesis of nanoparticles typically within an organic solvent and their posterior consolidation [34–36]. While the second route has obvious potential advantages in terms of cost, its cost-effectiveness is frequently limited by the use of organic solvents, and expensive precursors and additives, including surfactants and reducing/oxidizing agents [37,38]. Besides, the introduction of controlled amounts of electronic dopants by solution processing methods is not straightforward.

Here, we present a simple, fast, high yield and scalable synthesis route to produce PbS nanoparticles at ambient temperature, atmosphere and pressure, and within an aqueous solution. The proposed route is based on the stoichiometric reaction of ammonium sulfide and a metal salt, and takes advantage of the high reactivity of $(NH_4)_2S$ to produce small size nanoparticles even at room temperature and without the need for surfactants. Nanoparticles are then spark plasma sintered into compact polycrystalline materials. Using the same strategy, $Pb_{1-x}Cu_xS$ polycrystalline materials are produced and their thermoelectric properties are characterized. Results show the strong effect of Cu doping and the processing parameters on the thermoelectric properties of the resulting materials, which upon optimization, reach record thermoelectric figures of merit.

2. Material and methods

2.1 Chemicals

Lead(II) acetate trihydrate ($Pb(CH_3COO)_2 \cdot 3H_2O$), copper(II) nitrate trihydrate ($Cu(NO_3)_2 \cdot 3H_2O$), and ammonium sulfide solution ($(NH_4)_2S$, 20% in H_2O) were purchased from Fisher. All chemicals were used as received, without further purification.

2.2 Synthesis of PbS and $Pb_{1-x}Cu_xS$ nanoparticles

All reactions were carried out under ambient temperature, pressure and atmosphere in a fume hood. To produce PbS nanoparticles, first, 5 g $Pb(CH_3COO)_2 \cdot 3H_2O$ was dissolved with the help of ultrasounds in 100 mL of deionized water inside a bottle. The lead precursor solution was colourless and transparent. Second, 5 mL of an $(NH_4)_2S$ aqueous solution was injected into the lead precursor solution. Upon injection of the $(NH_4)_2S$ solution, $(NH_4)_2S$ stoichiometrically reacts with $Pb(CH_3COO)_2$ resulting in the instantaneous precipitation of PbS nanoparticles according to:

$$(NH_4)_2S + Pb(CH_3COO)_2 \rightarrow PbS + 2(NH_4)(CH_3COO)$$

The produced PbS was separated by centrifugation and washed two times with H_2O and two additional times with ethanol. The product was finally dried under vacuum for 2 hours at room temperature.

To produce $Pb_{1-x}Cu_xS$ nanoparticles, 5 × (1-x) mmol $Pb(CH_3COO)_2$ and 5x mmol $Cu(NO_3)_2$ were dissolved into 50 mL of deionized water in a bottle to form a light blue transparent uniform precursor. Then 2 mL of the $(NH_4)_2S$ aqueous solution was injected into the mixture solution. The obtained $Pb_{1-x}Cu_xS$ nanoparticles were centrifugated and washed few times, and then dried and stored.

2.3 Bulk nanomaterial consolidation

PbS and $Pb_{1-x}Cu_xS$ pellets were produced by first annealing the dried nanoparticles at 600°C for 180 min under a flow of reducing gas (95%Ar+5%H_2) inside a tube furnace. The heating rate was set at around 10 °C/min. Then, the annealed material was grounded into a fine powder

with an agate mortar, and loaded into a graphite die within the glovebox. The sintering process was carried out under vacuum using an AGUS PECS spark plasma sintering (SPS) system model SPS 210Sx to simultaneously apply to the sample a pressure of 45 MPa and a temperature of 600 ℃ for 5 min. The relative densities of the compacted pellets were measured by Archimedes' method.

2.4 Structural and chemical characterization

X-ray diffraction (XRD) patterns were measured on a Bruker AXS D8 Advance X-ray diffractometer with Cu−Kα radiation (λ = 1.5406 Å). An Auriga Zeiss field emission scanning electron microscope (SEM) operated at 5.0 kV was used to determine the particle size and morphology. Energy-dispersive X-ray spectroscopy (EDX) on an Oxford spectrometer attached to a Zeiss Auriga SEM at 20.0 kV was used to measure the material composition. Transmission electron microscopy (TEM) and high-resolution TEM (HRTEM) analyses were carried out under the 200 keV Tecnai F20 field emission microscope, using an embedded Gatan quantum image filter. X-ray photoelectron spectroscopy (XPS) was performed on the Specs system equipped with a Mg anode XR50 source, using a working power of 250 W, and a Phoibos 150 MCD-9 detector. The pressure in the analysis chamber was kept below 10^{-7} Pa. Data was processed using the CasaXPS software.

2.5 Thermoelectric property measurements

The Seebeck coefficient and electrical conductivity were simultaneously measured under helium atmosphere in an LSR-3 Linseis system. All samples were tested for at least three heating and cooling cycles. Considering the system and measurement accuracy, we estimated

the measurement error of the electrical conductivity and Seebeck coefficient to be about 4%. Thermal conductivities were obtained by multiplying the thermal diffusivity (λ), the constant pressure heat capacity (C_p), and the density of the material (ρ): $\kappa_{total} = \lambda C_p \rho$. Thermal diffusivities were measured on a xenon flash apparatus XFA600 and a laser flash analyzer LFA 1000 (Linseis), which have an estimated error of *ca*. 5 %. The heat capacity was estimated from the Dulong–Petit limit (3R law). The room temperature Hall charge carrier concentration (n_H) and mobility (μ_H) were measured by the Van der Pauw method under a magnetic field of 0.6 T on an ezHEMS, NanoMagnetics. Values provided correspond to the average of 6 measurements and the estimated error is ca. 10%. The high temperature n_H and μ_H were measured on a LINSEIS HCS 10, under a magnetic field of 1T.

3. Results and discussions

3.1. PbS nanoparticles

As schematized in Figure 1, lead sulfide nanoparticles were produced with a 98% material yield from the reaction of $(NH_4)_2S$ and $Pb(CH_3COO)_2 \cdot 3H_2O$ in water at ambient temperature, pressure and atmosphere (see the experimental section for details).

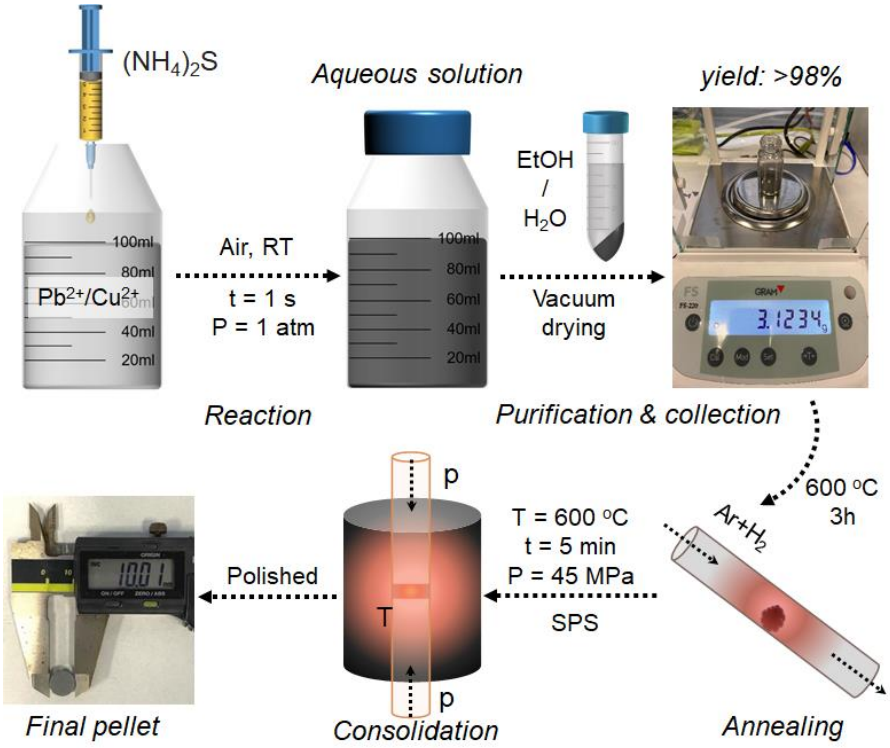

Figure 1. Schematic illustration of the process used to produce PbS and $Pb_{1-x}Cu_xS$ pellets. The whole process involves several steps: First, nanoparticles are produced from the reaction of $Pb(CH_3COO)_2 \cdot 3H_2O$ and the proper amount of $Cu(NO_3)_2 \cdot 3H_2O$ with $(NH_4)_2S$ in an aqueous solution at ambient pressure and temperature. The particles are precipitated, collected and dried. The nanopowder is afterwards annealed at 600 ºC for 3h under an Ar/H_2 atmosphere. Finally, the obtained powder is spark plasma sintered at 873 K and 45 MPa to obtain pellets with a diameter of 10 mm a 1.2 mm thickness and a relative density of ca. 95%.

TEM analysis showed the PbS particles to have a quasi-spherical geometry with an average size of around 18±5 nm (Figure 2a,b). The relatively high concentration of the solution and the very fast reaction of the Pb ions with the ammonium sulfide generates a high concentration of nucleus that consume most of the precursor and thus limit the growth of the nucleated crystals.

The relatively low reaction temperature also inhibits the Ostwald ripening of the particles, overall resulting in aggregated but nanometric size particles without the use of any capping ligand [39,40].

XRD patterns showed the particles to have a highly crystalline cubic PbS structure (JCPDS No. 01-077-0244, Figure 2c). From the Scherrer analysis of the XRD pattern, the size of the crystal domains was estimated at 17 nm, which is consistent with the average size obtained from TEM analysis. HRTEM characterization confirmed the excellent crystallinity and the PbS cubic structure (space group = FM3-M) with a=b=c=5.9360 Å (Figure 2d). EELS chemical composition maps showed Pb and S to be uniformly distributed across the nanoparticles (Figure 2e).

The high resolution Pb 4f XPS spectrum of PbS nanoparticles was fitted with two doublets (Figure S1a), which were associated with Pb^{2+} within a PbS chemical environment (Pb $4f_{7/2}$ binding energy at 137.3 eV) and a PbO environment (Pb $4f_{7/2}$ binding energy at 138.5 eV) [41]. The S 2p XPS spectrum of PbS nanoparticles (Figure S1b) was fitted with one doublet associated with S^{2-} within the PbS lattice (S $2p_{3/2}$ at 160.88 eV) [42]. Overall, the XPS analysis indicated the nanoparticles to be mainly composed of PbS with a minor PbO component originated during the exposure of the nanoparticles to air during handling and transportation.

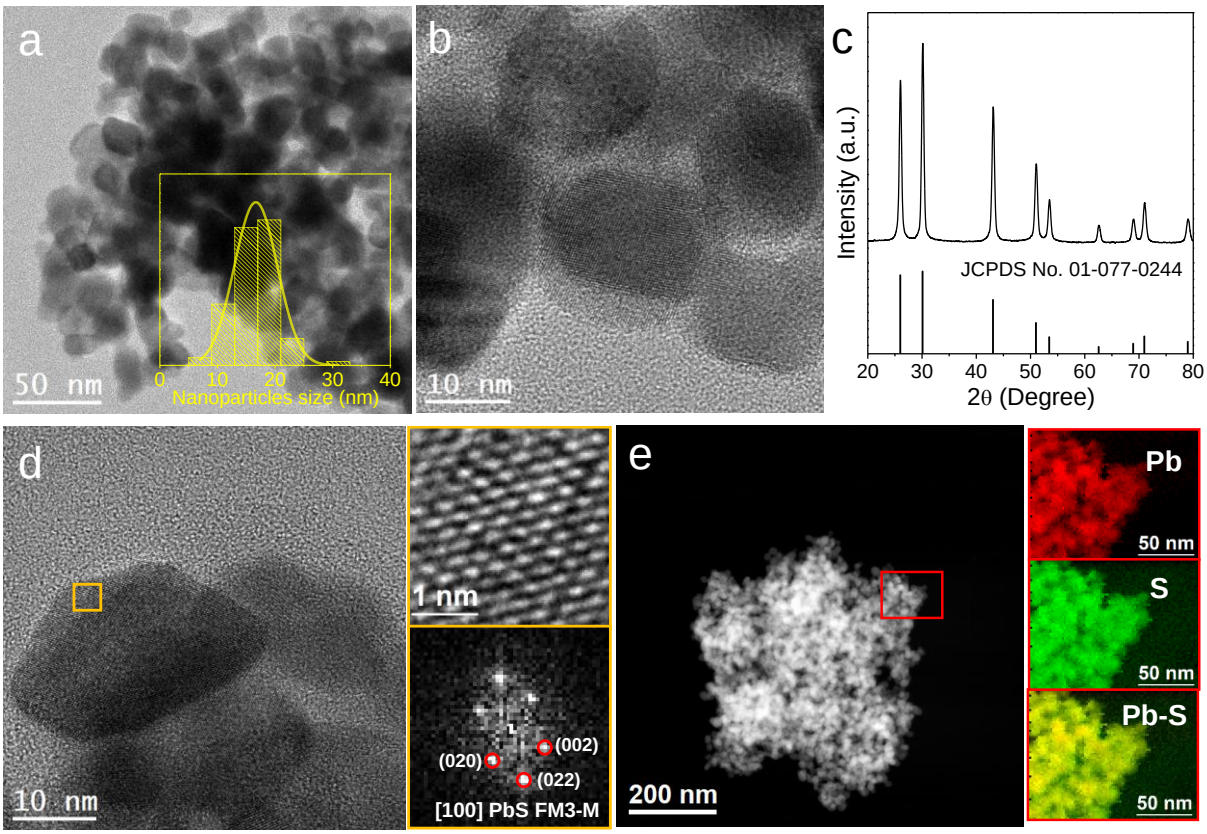

Figure 2. a-b) Representative TEM micrographs of PbS nanoparticles and histogram of the particle size distribution (inset). c) XRD pattern from PbS nanoparticles. d) HRTEM micrograph, detail of the orange squared region and its corresponding power spectrum. PbS lattice fringe distances were measured to be 0.284 nm, 0.202 nm, and 0.306 nm, at 45.82º and 88.31º which was interpreted as the cubic PbS phase, visualized along its [100] zone axis. e) STEM micrograph and EELS chemical composition maps obtained from the red squared area of the STEM micrograph. Individual Pb $N_{4,5}$-edge at 413 eV (red), S $L_{2,3}$-edge at 165 eV (green) and its composite.

3.2. Thermoelectric properties of PbS

PbS is intrinsically an n-type semiconductor owing to the presence of S vacancies [43–45]. PbS is prone to oxidation when exposed to air, which hampers its thermoelectric performance because the formed oxide, PbO, has a p-type conductivity [46–50]. Thus, to optimize the

thermoelectric properties of the material, the surface PbO need to be removed by annealing the material in a reducing atmosphere [51], as detailed in the experimental section. Upon annealing, XRD peaks became sharper, consistent with the growth of the crystallographic domains, with no additional crystalline phase being formed (Figure S2). SEM-EDX analysis confirmed the growth of the particles during the annealing step and showed the S content to decrease slightly (Figure S3). The annealed PbS was subsequently loaded into a 10 mm graphite die and spark plasma sintered at 600 °C and 45 MPa for 5 min under vacuum. The relative density of the obtained pellet was *ca*. 95% of the theoretical value, as measured by Archimedes' method. Cross-section SEM characterization showed the size of the crystal domains within the SPS material to be significantly larger (~ 0.4 μm) than the precursor PbS nanoparticles (Figure 3a and Figure S4).

As expected, the pellet obtained from the annealed PbS particles displayed a much higher electrical conductivity than a pellet produced from unannealed PbS, especially in the low temperature range (Figure 3b). This increase of electrical conductivity is mainly related to the increase of charge carrier concentration associated with the sulfur vacancies generated during the annealing process and an increase of mobility related to the removal of the oxide layer. Besides, the pre-annealed material displayed a negative Seebeck coefficient in the whole temperature range, while the unannealed reference pellet was characterized by a positive Seebeck coefficient at temperatures below 500 K and a negative *S* at higher temperatures, associated with the coexistence of both p-type PbO and n-type PbS (Figure 3c). The higher electrical conductivity and absolute Seebeck coefficients of the pre-annealed material resulted in much higher power factors, up to 1.1 $mWm^{-1}K^{-2}$. On the other hand, the lattice thermal

conductivity increased after annealing in a reducing atmosphere, which is related to the lower phonon scattering at grain boundaries with the disappearance of the lead oxide layer (Figure 3d). Overall, the pre-annealed material displayed significantly higher thermoelectric figures of merit than the unannealed reference pellet (Figure 3e). Thus, to investigate the effect of Cu, a pre-annealing step was considered for all the samples.

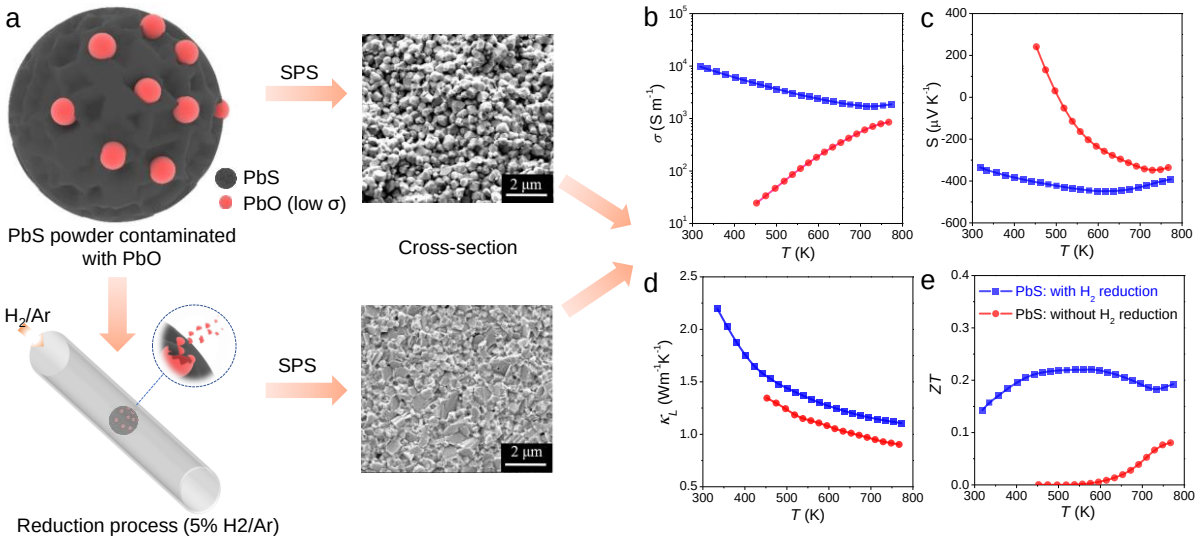

Figure 3. a) Schematic illustration of the oxide removal process, including cross-section SEM micrographs of the PbS pellets. b) Electrical conductivity, σ. c) Seebeck coefficient, S. d) Lattice thermal conductivity, κ_L. e) Thermoelectric figure of merit, ZT.

3.3. $Pb_{1-x}Cu_xS$ nanoparticles

$Pb_{1-x}Cu_xS$ nanoparticles were produced by the reaction of proper amounts of $Pb(CH_3COO)_2$ and $Cu(NO_3)_2$ with $(NH_4)_2S$ in water and at ambient temperature, pressure and atmosphere. With the Cu introduction, the geometry of the particles became less defined (Figure 4). The XRD pattern of the $Pb_{1-x}Cu_xS$ nanopowders displayed the cubic PbS phase, with no evidence of any additional peak corresponding to a Cu_xS phase (Figure S5). No systematic XRD peak

shift could be correlated with the amount of Cu introduced, but an evident widening of the diffraction peaks with the presence of Cu pointed towards a more defective crystal structure and/or a decrease in the size of the crystal domains. Using the Scherrer equation, the crystal domain size of the particles was observed to decrease with the amount of Cu, from 15.6 nm for $Pb_{0.992}Cu_{0.008}S$, to 7.6 nm for $Pb_{0.925}Cu_{0.075}S$ (Table S1).

Within the experimental error of the technique, SEM-EDX analysis showed the amount of copper within the material to correlate well with the nominal amount introduced (Table S1). EELS elemental composition maps showed a uniform distribution of the three elements, Pb, S and Cu. However, an exhaustive HRTEM characterization of the samples containing a larger amount of Cu, revealed not only the PbS cubic phase, but also crystal domains with a CuS hexagonal phase (Figure 4).

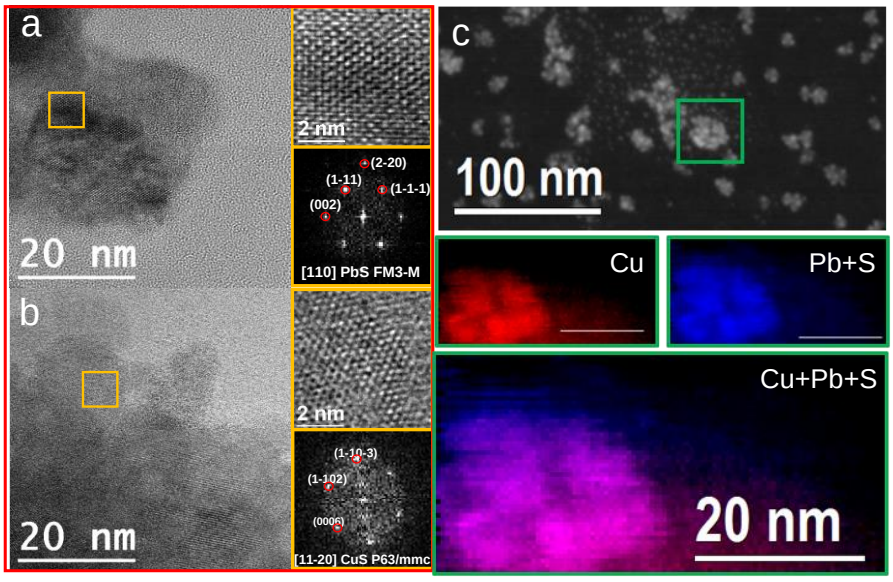

Figure 4. a,b) HRTEM micrographs of a $Pb_{0.955}Cu_{0.045}S$ sample, details of the orange squared regions and their corresponding power spectrum. c) STEM micrograph and EELS chemical composition maps of a $Pb_{0.955}Cu_{0.045}S$ sample.

All $Pb_{1-x}Cu_xS$ samples were annealed in an Ar/H_2 atmosphere at 600 ºC for 3 h. Subsequently, the annealed powders were consolidated into $Pb_{1-x}Cu_xS$ pellets by means of SPS sintering. The relative density of the $Pb_{1-x}Cu_xS$ pellets was similar to that of the PbS pellet, at *ca.* 96%. The XRD pattern of the sintered materials (Figure S6) displayed only the peaks corresponding to the PbS cubic phase. The presence of Cu caused a shift of the diffraction pattern to higher 2θ diffraction angles (Figure S6 and S7), which suggests the incorporation of the smaller Cu ions at Pb sites. This shift of the PbS diffraction peaks was partially correlated with the amount of Cu introduced, but it was more evident for the lowest doped materials. We speculate that while at low concentrations Cu incorporates at Pb sites, at higher concentrations, Cu could incorporate in different locations within the lattice, having opposite effects on the lattice parameters, e.g. intestinal copper would expand the lattice. Besides, at high concentrations, part of the Cu could segregate in the form of small and/or poorly crystalline Cu_xS domains that were not detected by XRD. Cross-section SEM-EDX and EELS elemental maps revealed a homogeneous distribution of the three elements, Pb, Cu and S, within the pellets (Figures S8 and S9).

3.4. Thermoelectric properties of $Pb_{1-x}Cu_xS$

As shown in Figure 5, all $Pb_{1-x}Cu_xS$ samples showed a monotonous decrease of electrical conductivity with temperature, denoting a degenerated semiconductor behaviour. $Pb_{1-x}Cu_xS$ samples were characterized by negative Seebeck coefficients in the whole temperature range measured, pointing at electrons as the majority charge carriers. All $Pb_{1-x}Cu_xS$ pellets displayed significantly larger electrical conductivities than PbS, but lower absolute values of the Seebeck coefficient. We associate these experimental observations with an increase of the charge carrier concentration with the introduction of Cu. Hall measurements quantified this increase of the

charge carrier concentration in approximately one order of magnitude, from n=1.8×10^{18} cm^{-3} for PbS to *ca.* n=1.0-2.5×10^{19} for $Pb_{1-x}Cu_xS$ (Table S2). The increase of the charge carrier concentration with the Cu introduction points at interstitial Cu atoms or the concomitant formation of S vacancies as having the main electronic role. Somehow surprisingly, the Hall charge carrier concentration did not correlate well with the amount of Cu introduced, but the increase of carrier concentration saturated at moderate Cu loadings. This saturation of the charge carrier concentration may be related to a saturation of the amount of Cu inserted within the PbS lattice or to the presence of Cu at different locations and playing opposite electronic roles.

As expected, the charge carrier mobility decreased with the presence of Cu, up to a factor three with respect to that of PbS, which is related to the presence of more charge scattering defects. However, surprisingly, the charge carrier mobility increased with the amount of Cu introduced (Table S2). This increase of the charge carrier mobility with the amount of Cu, with respect to the lowest Cu concentration introduced, could be related to the segregation of domains of Cu_xS secondary phases having large charge carrier concentrations and thus facilitating the transport of electrons [32,33]. Overall, the best power factors were obtained for the $Pb_{0.955}Cu_{0.045}S$ sample and reached a record value of 2.3 $mWm^{-1}K^{-2}$ at ambient temperature (Figure 5c).

Using the single parabolic band (SPB) model, we calculated the effective mass (m^*) of the $Pb_{1-x}Cu_xS$ materials from the following equation of the Seebeck coefficient:

$$S = \frac{8\pi^2 k_B^2}{3eh^2} m^* T \left(\frac{\pi}{3n_H}\right)^{\frac{2}{3}} \quad (1)$$

where k_B is the Boltzmann constant, h is the Planck constant, e is the elemental charge, n_H is

the charge carrier concentration, and m^* is the effective mass [52]. The calculated m^* increased with Cu doping, from $0.53m_0$ in PbS to $0.96m_0$ in $Pb_{0.955}Cu_{0.045}S$ (Figure 5d and Table S2).

Figure 5e displays a Pisarenko plot of the Seebeck coefficient and charge carrier concentration of all the samples at room temperature. The Seebeck coefficient of the Cu-doped samples was systematically above the theoretical curve plotted considering the effective m^* obtained from PbS.

The weighted carrier mobility (μ_w) was calculated from the electrical conductivity and Seebeck coefficient data:[8,52]

$$\mu_W = \frac{3\sigma}{8\pi e F_0(\eta)} \left(\frac{h^2}{2m_0 k_B T}\right)^{3/2} \quad (2)$$

where $F_n(\eta)$ is the Fermi integral with n=0 and is defined as:

$$F_n(\eta) = \int_0^\infty \frac{x^n}{1+e^{x-\eta}} dx \quad (3)$$

$$S = \pm \frac{K_B}{e} \left\{ \frac{(r+5/2)F_{r+3/2}(\eta)}{(r+3/2)F_{r+1/2}(\eta)} - \eta \right\} \quad (4)$$

where r denotes the scattering factor and η is the reduced chemical potential. We considered r=-1/2 owing to the dominant role of the acoustic scattering mechanism [53]. All the Cu-doped pellets show higher μ_w than pure PbS above 450 K. The enhancement on μ_w is especially significant for the $Pb_{0.955}Cu_{0.045}S$ pellet, which reached a value up to ~ 235 $cm^2V^{-1}s^{-1}$.

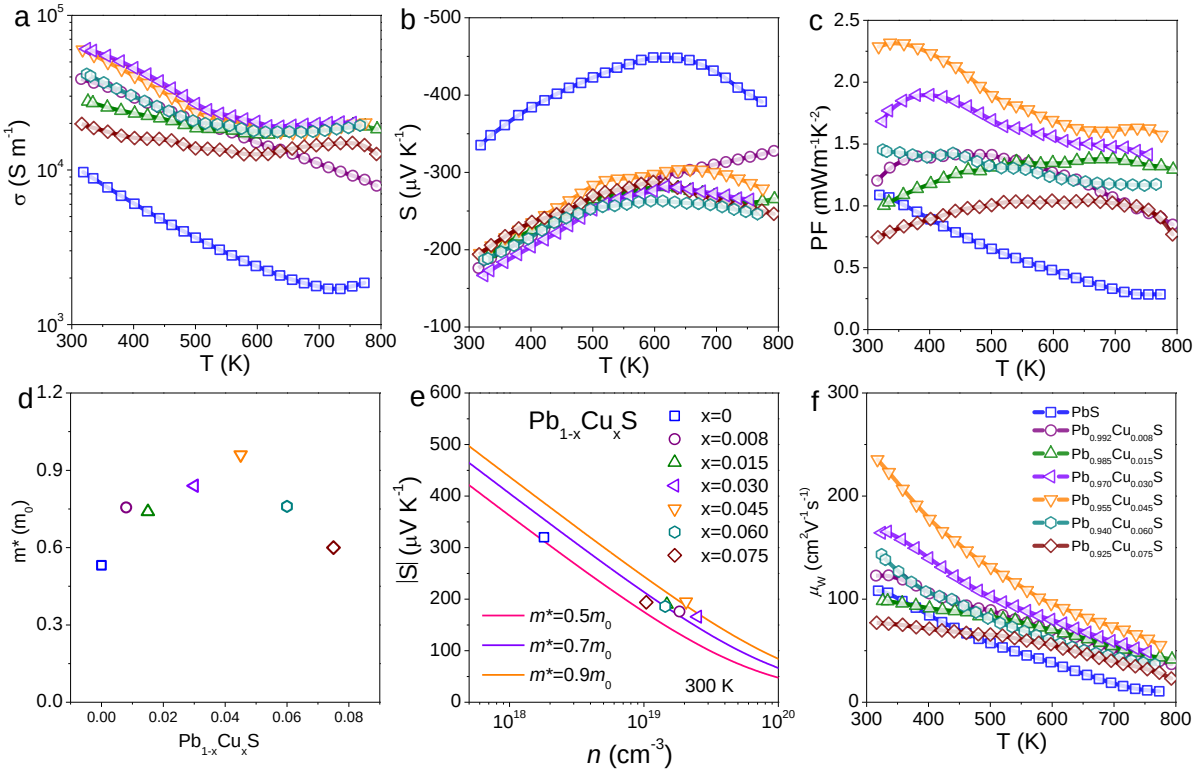

Figure 5. Thermoelectric properties of PbS and $Pb_{1-x}Cu_xS$ pellets: a) electrical conductivity, σ; b) Seebeck coefficient, S; c) power factor, PF; d) effective mass; e) Pisarenko relationship considering the effective mass at room temperature; and d) weighted mobility, μ_w.

Figure 6a,b shows the temperature dependence of the charge carrier concentration and mobility of the PbS and $Pb_{0.955}Cu_{0.045}S$ pellets. The carrier concentration of $Pb_{0.955}Cu_{0.045}S$ was systematically higher than that of PbS over the entire temperature range. Besides, while the carrier concentration of PbS was relatively stable throughout the whole temperature range analyzed, the carrier concentration of $Pb_{0.955}Cu_{0.045}S$ increased at temperatures above 600 K to reach ~8.7×10^{19} at 773 K. On the other hand, the carrier mobility of both samples monotonously decreased with increasing temperature, and the decrease was more accentuated for the Cu-doped material, especially above 600 K. This increase of charge carrier density and decrease of mobility can be related to the ionization of Cu-related impurities in this temperature range, thus

providing additional free electrons and accentuating charge carrier scattering.

Figure 6c,d displays the Pisarenko relationship at 773 K and the *n*-dependent *ZT* values at 773 K of PbS and $Pb_{0.955}Cu_{0.045}S$ pellets. The Pisarenko relationship shows that Seebeck coefficients of $Pb_{0.955}Cu_{0.045}S$ are systematically above those of PbS owing to the larger m* obtained through Cu doping. Besides, the calculated *n*-dependent *ZT* values show that a maximum *ZT* at $n \sim 1.15 \times 10^{20}$ cm^{-3} for $Pb_{0.955}Cu_{0.045}S$ at 773 K, which is close to our experimental value (8.7×10^{19} cm^{-3}). Thus, the *ZT*~1.22 at 773 K experimental obtained here for $Pb_{0.955}Cu_{0.045}S$ is very close to the maximum that can be reached in this system as calculated within the framework of the SPB model. The SPB model also showed the PbS to follow a similar trend but with a maximum *ZT* at a lower charge carrier concentration of *ca.* 4.5×10^{19} cm^{-3}.

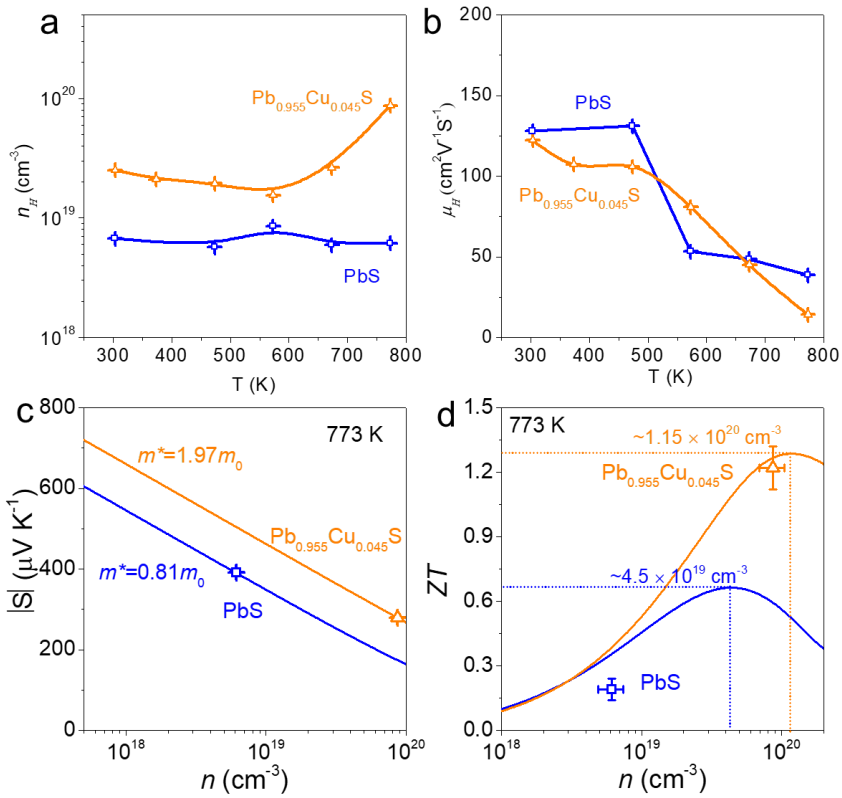

Figure 6. a) Temperature dependence of carrier concentration, n_H; b) Temperature dependence of carrier

mobility, μ_H; c) Pisarenko relationship considering the effective masses calculated at 773 K; and d) *n*-dependence of *ZT* values at 773 K for PbS and $Pb_{0.955}Cu_{0.045}S$ pellets.

The thermal conductivity monotonously decreased with temperature (Figure 7a). It was similar for all the measured samples due to the compensation of the larger electronic contribution of the Cu-doped materials associated with their larger charge carrier concentration, by a potentially lower lattice component compared with pure PbS. Indeed, when subtracting the electronic contribution to the thermal conductivity, we observed the lattice thermal conductivity of the $Pb_{1-x}Cu_xS$ samples to be systematically lower than that of PbS, which is associated with the enhanced phonon scattering at Cu atomic impurities and potential Cu_xS secondary phases (Figure 7b).

The dimensionless thermoelectric quality factor *B* was calculated using the following equation:[10]

$$B = 9\frac{\mu_W}{k_{lat}}\left(\frac{T}{300}\right)^{5/2} \quad (5)$$

B increased with the Cu amount up to the $Pb_{0.955}Cu_{0.045}S$ pellet, which reached a very high quality factor of 1.5×10^3 at 320 K and 8.0×10^3 at 773 K (Figure 7c).

Overall, record *ZT* values were obtained from $Pb_{0.955}Cu_{0.045}S$ samples, reaching *ZT*=1.22 at 773 K, which is about 4 times higher than that of undoped PbS (Figure 7d). To the best of our knowledge, the power factor 2.3 $mWm^{-1}K^{-2}$ and *ZT* = 0.37 obtained at room temperature from $Pb_{0.955}Cu_{0.045}S$ samples are the highest reported for an n-type PbS-based material (Figure 8). In addition, a record *ZT* average, ZT_{avg} = 0.76, was obtained in the temperature range from 320 K to 773 K.

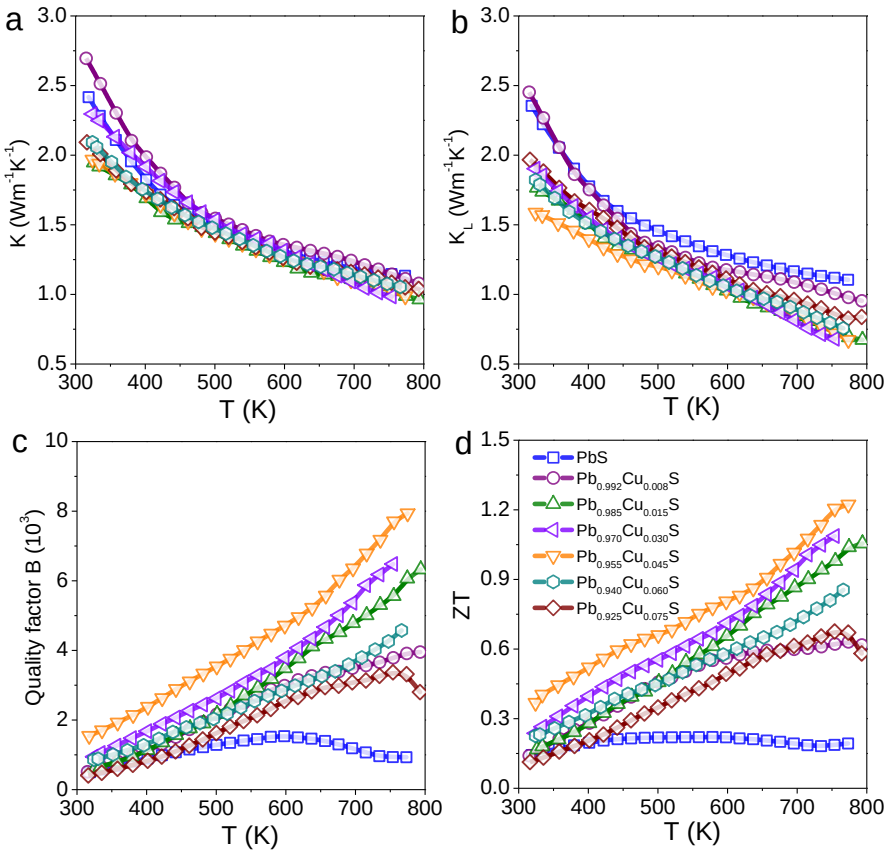

Figure 7. Thermoelectric properties of $Pb_{1-x}Cu_xS$ nanomaterials: a) thermal conductivity, κ b) lattice thermal conductivity, κ_L; c) quality factor, *B* and d) figure of merit, *ZT*.

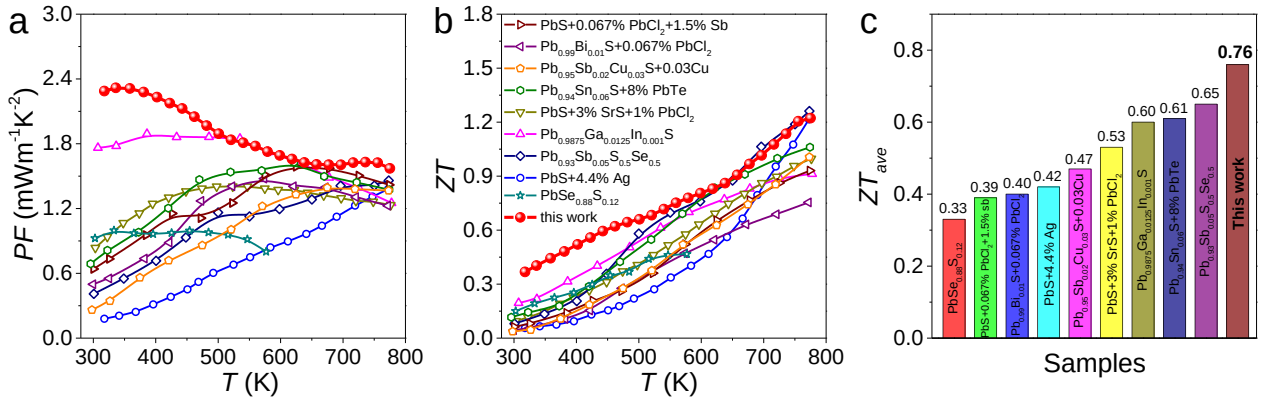

Figure 8. Comparison of thermoelectric performance of the $Pb_{0.955}Cu_{0.045}S$ sample with state-of-the-art n-type PbS-based materials [5,9,15,20,22,24,26,54,55]: a) PF; b) *ZT*; c) ZT_{ave} (320-773 K).

4. Conclusion

We reported a facile, rapid, scalable and low-cost method for the synthesis of PbS and $Pb_{1-x}Cu_xS$ nanoparticles in aqueous media and at ambient temperature, pressure and atmosphere. The nanoparticles were annealed under a reducing atmosphere to remove surface PbO and spark plasma sintered to obtain pellets with 95% relative density. The incorporation of Cu ions resulted in an increase of electrical conductivity and effective mass that translated into higher power factors compared with bare PbS. The presence of Cu also caused a decrease in the lattice thermal conductivity over the whole temperature range. These improved properties resulted in higher *ZT* values, up to 1.22 at 773 K for $Pb_{0.985}Cu_{0.15}S$, which is about fourfold higher than undoped PbS. Besides, a $ZT = 0.37$ at room temperature and a $ZT_{avg} = 0.76$ from 320 K to 773 K obtained from $Pb_{0.955}Cu_{0.045}S$ samples are the highest reported for an n-type PbS-based material.

Declaration of Competing Interest

The authors declare that they have no known competing financial interests or personal relationships that could have appeared to influence the work reported in this paper.

Acknowledgment

This work was supported by the European Regional Development Funds. MYL, YZ, DWY and KX thank the China Scholarship Council for scholarship support. Y.L. acknowledges funding from the European Union's Horizon 2020 research and innovation program under the Marie Sklodowska-Curie grant agreement No. 754411. CC and MI acknowledge funding from IST

Austria and the Werner Siemens Foundation. C.C. acknowledges funding from the FWF “Lise Meitner Fellowship” grant agreement M 2889-N. TZ has received funding from the CSC-UAB PhD scholarship program. ICN2 acknowledges funding from Generalitat de Catalunya 2017 SGR 327. ICN2 thanks support from the project NANOGEN (PID2020-116093RB-C43), funded by MCIN/ AEI/10.13039/501100011033/.. ICN2 is supported by the Severo Ochoa program from Spanish MINECO (Grant No. SEV-2017-0706) and is funded by the CERCA Programme / Generalitat de Catalunya. Part of the present work has been performed in the framework of Universitat Autònoma de Barcelona Materials Science PhD program.

References

[1] X.L. Shi, J. Zou, Z.G. Chen, Advanced thermoelectric design: From materials and structures to devices, Chem. Rev. 120 (2020) 7399–7515.

[2] Y. Wang, L. Yang, X.L. Shi, X. Shi, L. Chen, M.S. Dargusch, J. Zou, Z.G. Chen, Flexible Thermoelectric Materials and Generators: Challenges and Innovations, Adv. Mater. 31 (2019) 1–47.

[3] L. Yang, Z.G. Chen, M.S. Dargusch, J. Zou, High Performance Thermoelectric Materials: Progress and Their Applications, Adv. Energy Mater. 8 (2018) 1–28.

[4] Z.G. Chen, X. Shi, L.D. Zhao, J. Zou, High-performance SnSe thermoelectric materials: Progress and future challenge, Prog. Mater. Sci. 97 (2018) 283–346.

[5] M. Ibáñez, Z. Luo, A. Genç, L. Piveteau, S. Ortega, D. Cadavid, O. Dobrozhan, Y. Liu, M. Nachtegaal, M. Zebarjadi, J. Arbiol, M. V. Kovalenko, A. Cabot, High-performance thermoelectric nanocomposites from nanocrystal building blocks, Nat. Commun. 7

(2016) 1–7.

[6] M. Ibáñez, R.J. Korkosz, Z. Luo, P. Riba, D. Cadavid, S. Ortega, A. Cabot, M.G. Kanatzidis, Electron doping in bottom-up engineered thermoelectric nanomaterials through HCl-mediated ligand displacement, J. Am. Chem. Soc. 137 (2015) 4046–4049.

[7] C.M. Zeuthen, P.S. Thorup, N. Roth, B.B. Iversen, Reconciling crystallographic and physical property measurements on thermoelectric lead sulfide, J. Am. Chem. Soc. 141 (2020) 8146–8157.

[8] Y. Xiao, D. Wang, Y. Zhang, C. Chen, S. Zhang, K. Wang, G. Wang, S.J. Pennycook, G.J. Snyder, H. Wu, L.D. Zhao, Band Sharpening and Band Alignment Enable High Quality Factor to Enhance Thermoelectric Performance in n-Type PbS, J. Am. Chem. Soc. 142 (2020) 4051–4060.

[9] J. Yang, X. Zhang, G. Liu, L. Zhao, J. Liu, Z. Shi, J. Ding, G. Qiao, Multiscale structure and band configuration tuning to achieve high thermoelectric properties in n-type PbS bulks, Nano Energy. 74 (2020) 104826.

[10] Y. Pei, H. Wang, G.J. Snyder, Band engineering of thermoelectric materials, Adv. Mater. 24 (2012) 6125–6135.

[11] B. Xu, T. Feng, M.T. Agne, Q. Tan, Z. Li, K. Imasato, L. Zhou, J.-H. Bahk, X. Ruan, G.J. Snyder, Y. Wu, Manipulating Band Structure through Reconstruction of Binary Metal Sulfide for High-Performance Thermoelectrics in Solution-Synthesized Nanostructured $Bi_{13}S_{18}I_2$, Angew. Chemie. 130 (2018) 2437–2442.

[12] S. Johnsen, J. He, J. Androulakis, V.P. Dravid, I. Todorov, D.Y. Chung, M.G. Kanatzidis, Nanostructures boost the thermoelectric performance of PbS, J. Am. Chem. Soc. 133 (2011) 3460–3470.

[13] Y. Li, J. Lin, H. Xie, Y. Wang, Z. Li, Raising the thermoelectric performance of PbS with low-content polyparaphenylene, J. Mater. Sci. Mater. Electron. 31 (2020) 6586–6592.

[14] Y. Qin, Y. Xiao, D. Wang, B. Qin, Z. Huang, L.D. Zhao, An approach of enhancing thermoelectric performance for p-type PbS: Decreasing electronic thermal conductivity, J. Alloys Compd. 820 (2020) 153453.

[15] L.D. Zhao, J. He, S. Hao, C.I. Wu, T.P. Hogan, C. Wolverton, V.P. Dravid, M.G. Kanatzidis, Raising the thermoelectric performance of p-type PbS with endotaxial nanostructuring and valence-band offset engineering using CdS and ZnS, J. Am. Chem. Soc. 134 (2012) 16327–16336.

[16] M. Ibáñez, R. Zamani, S. Gorsse, J. Fan, S. Ortega, D. Cadavid, J.R. Morante, J. Arbiol, A. Cabot, Core-shell nanoparticles as building blocks for the bottom-up production of functional nanocomposites: PbTe-PbS thermoelectric properties, ACS Nano. 7 (2013) 2573–2586.

[17] Y. Liu, M. Calcabrini, Y. Yu, S. Lee, C. Chang, J. David, T. Ghosh, M.C. Spadaro, C. Xie, O. Cojocaru-Mirédin, J. Arbiol, M. Ibáñez, Defect Engineering in Solution-Processed Polycrystalline SnSe Leads to High Thermoelectric Performance, ACS Nano. (2021). doi:10.1021/acsnano.1c06720.

[18] Y. Liu, M. Calcabrini, Y. Yu, A. Genç, C. Chang, T. Costanzo, T. Kleinhanns, S. Lee, J.

Llorca, O. Cojocaru-Mirédin, M. Ibáñez, The importance of surface adsorbates in solution-processed thermoelectric materials: the case of SnSe, Adv. Mater. (2021) 2106858.

[19] D. Wu, L.D. Zhao, X. Tong, W. Li, L. Wu, Q. Tan, Y. Pei, L. Huang, J.F. Li, Y. Zhu, M.G. Kanatzidis, J. He, Superior thermoelectric performance in PbTe-PbS pseudo-binary: Extremely low thermal conductivity and modulated carrier concentration, Energy Environ. Sci. 8 (2015) 2056–2068.

[20] B. Liu, H. Ma, Q. Chen, Y. Wang, G. Ji, X. Li, Y. Zhang, X. Jia, Optimization and modulation for the moderate and high temperature thermoelectric properties of PbSe via solid solution with PbS synthesized by HPHT, Mod. Phys. Lett. B. 34 (2020) 1–9.

[21] M. Calcabrini, A. Genç, Y. Liu, T. Kleinhanns, S. Lee, D.N. Dirin, Q.A. Akkerman, M. V. Kovalenko, J. Arbiol, M. Ibáñez, Exploiting the Lability of Metal Halide Perovskites for Doping Semiconductor Nanocomposites, ACS Energy Lett. 6 (2021) 581–587.

[22] B. Jiang, X. Liu, Q. Wang, J. Cui, B. Jia, Y. Zhu, J. Feng, Y. Qiu, M. Gu, Z. Ge, J. He, Realizing high-efficiency power generation in low-cost PbS-based thermoelectric materials, Energy Environ. Sci. 13 (2020) 579–591.

[23] Z. Hou, D. Wang, T. Hong, Y. Qin, S. Peng, G. Wang, J. Wang, X. Gao, Z. Huang, L.D. Zhao, Boosting thermoelectric performance of n-type PbS through synergistically integrating In resonant level and Cu dynamic doping, J. Phys. Chem. Solids. 148 (2021) 109640.

[24] L. Zhao, J. Yang, B. Lu, X. Zhang, J. Hu, W. Xie, H. Shao, G. Liu, S. Hussain, Z. Shi, G.

Qiao, Enhanced thermoelectric properties of n-type Cl doped PbS-based materials via Bi alloying, J. Alloys Compd. (2020) 157788.

[25] Y. Liu, D. Cadavid, M. Ibáñez, S. Ortega, S. Martí-Sánchez, O. Dobrozhan, M. V. Kovalenko, J. Arbiol, A. Cabot, Thermoelectric properties of semiconductor-metal composites produced by particle blending, APL Mater. 4 (2016) 104813.

[26] M. Zhao, C. Chang, Y. Xiao, R. Gu, J. He, L.D. Zhao, Investigations on distinct thermoelectric transport behaviors of Cu in n-type PbS, J. Alloys Compd. 781 (2019) 820–830.

[27] L. You, Z. Li, Q. Ma, S. He, Q. Zhang, F. Wang, G. Wu, Q. Li, P. Luo, J. Zhang, J. Luo, High Thermoelectric Performance of Cu-Doped PbSe-PbS System Enabled by High-Throughput Experimental Screening, Research. 2020 (2020) 1–8.

[28] Y. Qin, D. Wang, Z. Hou, Y. Xiao, G. Wang, Z. Huang, L.D. Zhao, Thermoelectric transport properties of PbS and its contrasting electronic band structures, Scr. Mater. 185 (2020) 76–81.

[29] S.N. Girard, J. He, X. Zhou, D. Shoemaker, C.M. Jaworski, C. Uher, V.P. Dravid, J.P. Heremans, M.G. Kanatzidis, High performance Na-doped PbTe-PbS thermoelectric materials: Electronic density of states modification and shape-controlled nanostructures, J. Am. Chem. Soc. 133 (2011) 16588–16597.

[30] Y. Qin, T. Hong, B. Qin, D. Wang, W. He, X. Gao, Y. Xiao, L.D. Zhao, Contrasting Cu Roles Lead to High Ranged Thermoelectric Performance of PbS, Adv. Funct. Mater. 2102185 (2021) 1–9.

[31] M. Li, Y. Liu, Y. Zhang, X. Han, K. Xiao, M. Nabahat, J. Arbiol, J. Llorca, M. Iban, A. Cabot, PbS−Pb−Cu_xS Composites for Thermoelectric Application, ACS Appl. Mater. Interfaces. 13 (2021) 51373-51382.

[32] Y. Zhang, C. Xing, Y. Liu, M.C. Spadaro, X. Wang, M. Li, K. Xiao, T. Zhang, P. Guardia, K.H. Lim, A.O. Moghaddam, J. Llorca, J. Arbiol, M. Ibáñez, A. Cabot, Doping-mediated stabilization of copper vacancies to promote thermoelectric properties of $Cu_{2-x}S$, Nano Energy. 85 (2021) 105991.

[33] M. Li, Y. Liu, Y. Zhang, X. Han, T. Zhang, Y. Zuo, C. Xie, K. Xiao, J. Arbiol, J. Llorca, M. Ibáñez, J. Liu, A. Cabot, Effect of the Annealing Atmosphere on Crystal Phase and Thermoelectric Properties of Copper Sulfide, ACS Nano. 15 (2021) 4967-4978.

[34] M. Ibáñez, A. Genç, R. Hasler, Y. Liu, O. Dobrozhan, O. Nazarenko, M. De La Mata, J. Arbiol, A. Cabot, M. V. Kovalenko, Tuning transport properties in thermoelectric nanocomposites through inorganic ligands and heterostructured building blocks, ACS Nano. 13 (2019) 6572–6580.

[35] M. Kowshik, W. Vogel, J. Urban, S.K. Kulkarni, K.M. Paknikar, Microbial synthesis of semiconductor PbS nanocrystallites, Adv. Mater. 14 (2002) 815–818.

[36] I. Resa, H. Moreira, B. Bresson, B. Mahler, B. Dubertret, H. Aubin, Synthesis of monodisperse superconducting lead nanocrystals, J. Phys. Chem. C. 113 (2009) 7120–7122.

[37] Y. Zhang, C. Xing, Y. Liu, M. Li, K. Xiao, P. Guardia, S. Lee, X. Han, A. Ostovari Moghaddam, J. Josep Roa, J. Arbiol, M. Ibáñez, K. Pan, M. Prato, Y. Xie, A. Cabot,

Influence of copper telluride nanodomains on the transport properties of n-type bismuth telluride, Chem. Eng. J. 418 (2021) 129374.

[38] S. Ortega, M. Ibáñez, Y. Liu, Y. Zhang, M. V. Kovalenko, D. Cadavid, A. Cabot, Bottom-up engineering of thermoelectric nanomaterials and devices from solution-processed nanoparticle building blocks, Chem. Soc. Rev. 46 (2017) 3510–3528.

[39] M. Ibáñez, P. Guardia, A. Shavel, D. Cadavid, J. Arbiol, J.R. Morante, A. Cabot, Correction to Growth Kinetics of Asymmetric Bi_2S_3 Nanocrystals: Size Distribution Focusing in Nanorods , J. Phys. Chem. C. 115 (2011) 11888–11888.

[40] P.W. Voorhees, The theory of Ostwald ripening, J. Stat. Phys. 38 (1985) 231–252.

[41] V.M. Koch, M.K.S. Barr, P. Büttner, I. Mínguez-Bacho, D. Döhler, B. Winzer, E. Reinhardt, D. Segets, J. Bachmann, A solution-based ALD route towards $(CH_3NH_3)(PbI_3)$ perovskite: Via lead sulfide films, J. Mater. Chem. A. 7 (2019) 25112–25119.

[42] V. V. Burungale, R.S. Devan, S.A. Pawar, N.S. Harale, V.L. Patil, V.K. Rao, Y.R. Ma, J.E. Ae, J.H. Kim, P.S. Patil, Chemically synthesized PbS nanoparticulate thin films for a rapid NO_2 gas sensor, Mater. Sci. Pol. 34 (2016) 204–211.

[43] N. Mishra, G. Makov, Point defects in lead sulfide: A first-principles study, Comput. Mater. Sci. 190 (2021) 110285.

[44] D. Zherebetskyy, Y. Zhang, M. Salmeron, L.W. Wang, Tolerance of Intrinsic Defects in PbS Quantum Dots, J. Phys. Chem. Lett. 6 (2015) 4711–4716.

[45] L.A. Hemstreet, Cluster calculations of the effects of single vacancies of the electronic

properties of PbS, Phys. Rev. B. 11 (1975) 2260–2270.

[46] M.H. Zarghami, Y. Liu, M. Gibbs, E. Gebremichael, C. Webster, M. Law, P-type PbSe and PbS quantum dot solids prepared with short-chain acids and diacids, ACS Nano. 4 (2010) 2475–2485.

[47] E.J.D. Klem, H. Shukla, S. Hinds, D.D. MacNeil, L. Levina, E.H. Sargent, Impact of dithiol treatment and air annealing on the conductivity, mobility, and hole density in PbS colloidal quantum dot solids, Appl. Phys. Lett. 92 (2008) 1–4.

[48] E.I. Rogacheva, I.M. Krivulkin, O.N. Nashchekina, A.Y. Sipatov, V. V. Volobuev, M.S. Dresselhaus, Effect of oxidation on the thermoelectric properties of PbTe and PbS epitaxial films, Appl. Phys. Lett. 78 (2001) 1661–1663.

[49] Y. Cao, A. Stavrinadis, T. Lasanta, D. So, G. Konstantatos, The role of surface passivation for efficient and photostable PbS quantum dot solar cells, Nat. Energy. 1 (2016) 1–6.

[50] R.Y. Wang, J.P. Feser, J.S. Lee, D. V. Talapin, R. Segalman, A. Majumdar, Enhanced thermopower in PbSe nanocrystal quantum dot superlattices, Nano Lett. 8 (2008) 2283–2288.

[51] Y.K. Lee, Z. Luo, S.P. Cho, M.G. Kanatzidis, I. Chung, Surface Oxide Removal for Polycrystalline SnSe Reveals Near-Single-Crystal Thermoelectric Performance, Joule. 3 (2019) 719–731.

[52] B. Qin, W. He, L.D. Zhao, Estimation of the potential performance in p-type SnSe

crystals through evaluating weighted mobility and effective mass, J. Mater. 6 (2020) 671–676.

[53] L. Pan, S. Mitra, L.D. Zhao, Y. Shen, Y. Wang, C. Felser, D. Berardan, The Role of Ionized Impurity Scattering on the Thermoelectric Performances of Rock Salt $AgPbmSnSe_{2+m}$, Adv. Funct. Mater. 26 (2016) 5149–5157.

[54] Z.Z. Luo, S. Hao, S. Cai, T.P. Bailey, G. Tan, Y. Luo, I. Spanopoulos, C. Uher, C. Wolverton, V.P. Dravid, Q. Yan, M.G. Kanatzidis, Enhancement of Thermoelectric Performance for n-Type PbS through Synergy of Gap State and Fermi Level Pinning, J. Am. Chem. Soc. 141 (2019) 6403–6412.

[55] Z. Hou, Y. Qiu, D. Ren, Z. Huang, L.D. Zhao, Enhancing thermoelectric transport properties of n-type PbS through introducing CaS/SrS, J. Solid State Chem. 280 (2019) 120995.